



Porous heterojunction of Ni₂P/Ni₇S₆ with high crystalline phase and superior conductivity for industrial anion exchange membrane water electrolysis

Fu-Li Wang, Na Xu, Cheng-Jie Yu, Jing-Yi Xie, Bin Dong^{*}, Xin-Yu Zhang, Yi-Wen Dong, Yu-Lu Zhou, Yong-Ming Chai^{*}

State Key Laboratory of Heavy Oil Processing, College of Chemistry and Chemical Engineering, China University of Petroleum (East China), Qingdao 266580, PR China

ARTICLE INFO

Keywords:

Porous heterojunction
High crystalline phase
Superior conductivity
AEM water electrolysis
Molten salt

ABSTRACT

Limited by sluggish mass and charge transfer in anion exchange membrane (AEM) water electrolysis, designing high crystalline phase and superior conductivity electrocatalysts for oxygen evolution is crucial in promoting application of hydrogen. Herein, maple leaf-shaped porous heterojunction (Ni₂P/Ni₇S₆) is fabricated by one-step molten salt method. Benefited from rich porosity and high crystal structure, the target catalyst with abundant active sites and great mechanical strength only requires the overpotentials of 330 mV to reach 1000 mA cm⁻², and can sustain at 500 mA cm⁻² for 700 h. Besides, characterizations and theoretical calculations reveal that strong interaction between Ni₂P and Ni₇S₆ leads to a depleted electron density in Ni sites and optimizes the adsorption energy of *OOH and H₂O, achieving favorable kinetics and superior conductivity. Meanwhile, assembled AEM water electrolyzer delivers 1000 mA cm⁻² at a cell voltage of 1.88 V, operating at the average energy efficiency of 72 % for 140 h.

1. Introduction

Electrolytic water splitting driven by renewable energy (solar/wind) provides high-purity hydrogen to solve increasingly severe energy and environmental problems [1–3]. The main commercial hydrogen production methods are alkaline water electrolysis (AWE) and proton-exchange membrane (PEM). However, the high energy consumption in AWE and noble-metal electrocatalysts in PEM limit its large-scale commercial hydrogen production [4,5]. Anion exchange membrane (AEM) water electrolyzer is a promising industrial hydrogen production method with broad application prospects. It has the advantages of AWE and PEM, including using non-precious metal catalysts and efficient production of high-purity hydrogen [6,7]. To date, AEM water electrolysis is still in the initial stage. There is an urgent need to develop highly active and stable industrial electrocatalysts to meet the high-efficient AEM water electrolysis [8,9].

AEM water electrolysis consists of two half-reactions, including hydrogen evolution reaction (HER) and oxygen evolution reaction (OER), where the OER is a significant challenge due to its prolonged four-electron transfer process [10]. Currently, Ru- and Ir-based

materials are the benchmark OER electrocatalysts. Unfortunately, the high price and scarcity impede their widespread applications in AEM water electrolysis [11]. Many promising transition metal OER electrocatalysts have been developed in recent studies, such as metal sulfides, phosphides, oxides, and hydroxides [12–15]. Among them, Ni-based transition metal sulfides have attracted enormous attention because of their low price and abundant natural storage [16]. In particular, due to the mutual support between atoms, the high crystal transition metal sulfides could exhibit excellent mechanical strength and stability [17]. However, nickel sulfides with a high crystalline phase have a large energy barrier for OER intermediates, significantly limiting their OER activity [18]. The construction of a heterojunction interface could adjust the electronic structure, optimize the adsorption energy, and give full play to multi-component advantages, improving the OER catalytic performance [19,20]. For example, Li et al. reported that the NiS/NiO@N-C NT/NFs needed the overpotential of 269 mV to reach 10 mA cm⁻², and the electrode ran 25000 s at an overpotential of 300 mV [21]. Feng et al. reported that FeP/Ni₂P HNSs displayed the lowest overpotential of 234 mV at a current density of 10 mA cm⁻², and the electrocatalyst operated 20 h at an overpotential of 245 mV [22]. Although many researchers

^{*} Corresponding authors.

E-mail addresses: dongbin@upc.edu.cn (B. Dong), ymchai@upc.edu.cn (Y.-M. Chai).

<https://doi.org/10.1016/j.apcatb.2023.122633>

Received 29 November 2022; Received in revised form 13 February 2023; Accepted 12 March 2023

Available online 13 March 2023

0926-3373/© 2023 Elsevier B.V. All rights reserved.

have improved the OER performance for Ni-based sulfides by constructing heterojunctions, these synthesis steps are tedious and complex, which increases the cost of industrial-grade electrocatalysts and makes it difficult for large-scale industrial applications. More importantly, the traditional synthesis methods (hydrothermal and gas phase synthesis) are challenging to maintain the original high crystal phase structure in heterojunction, so it cannot meet the long-term stable operation. Therefore, it is still a great challenge to accurately and controllably construct the heterojunction catalyst with a high crystal phase structure through a simple method to make the catalyst meet the needs of high activity and stability for industrial AEM water electrolysis.

Based on the above analysis, the one-step molten salt method has successfully constructed a novel $\text{Ni}_2\text{P}/\text{Ni}_7\text{S}_6$ heterojunction with porous maple leaf nanosheets. Benefiting from the strong polarization in the unique molten environment, heterojunction with a high crystalline phase is still maintained after the precise introduction of P atoms, guaranteeing fast infiltration of electrolyte and outstanding mechanical strength at the high current catalysis. Beyond that, fast charge transfer in the heterointerface regulates the adsorption energy of $^*\text{OOH}$ intermediate and H_2O molecules for unusual OER activity and conductivity. As expected, the $\text{Ni}_2\text{P}/\text{Ni}_7\text{S}_6$ electrode exhibits impressive activity and stability toward OER with extremely low overpotentials of 304 and 330 mV to deliver a current density of 500 and 1000 mA cm^{-2} in alkaline media, and can operate stably at 500 mA cm^{-2} for 700 h. When assembled into AEM Water electrolysis ($\text{Ni}_2\text{P}/\text{Ni}_7\text{S}_6//(\text{Pt}/\text{C})$) for industrial application, the cell can achieve 1000 mA cm^{-2} at 1.88 V and stably work for 140 h maintaining 72 % energy efficiency.

2. Experimental section

The Ni foam with a thickness of 2 mm was purchased from Kunshan JiaYiSheng Electronics CO. LTD. All the reagents used in this paper were purchased from Aladdin Chemical Co. Ltd. (Shanghai, China) and directly used in the experiment without further separation and purification. The potassium thiocyanate (KSCN) was used as molten salt, acting as a reaction medium. SCN^- with a linear configuration can coordinate with transition metal ions via S ligands to form various complexes. Geometric structure of KSCN was presented in Fig. S1.

2.1. Synthesis of $\text{Ni}_2\text{P}/\text{Ni}_7\text{S}_6$

The heterojunction structure of $\text{Ni}_2\text{P}/\text{Ni}_7\text{S}_6$ was prepared for the first time by the one-step molten salt method. First of all, a piece of Ni foam ($1\text{ cm} \times 2\text{ cm}$) was washed by ultrasound in 0.5 M H_2SO_4 , acetone, and ethanol for 30 min, respectively, to remove oxides and impurities on the surface. The cleaned Ni foam was transferred to a vacuum drying oven at 60 °C for 24 h. Subsequently, the ball mill was used to evenly mix 5 g KSCN and 1 g NaH_2PO_2 . And we put the processed Ni foam at the bottom of the porcelain boat ($10 \times 20 \times 3\text{ mm}$) and covered the surface with mixed salt. Next, the porcelain boat was heated at 250 °C for 2 h in a well-sealed tubular furnace with a heating rate of 5 °C min^{-1} under the Ar atmosphere. After cooling to room temperature, the salt in the porcelain boat became a yellow-white solid. After washing with a large amount of Deionized (DI) water, the $\text{Ni}_2\text{P}/\text{Ni}_7\text{S}_6$ with black color was obtained and dried in the vacuum oven at 60 °C for 24 h.

2.2. Synthesis of Ni_7S_6

A similar molten salt method can be performed to synthesize Ni_7S_6 directly. Firstly, the treated Ni foam was covered with 5 g KSCN in the porcelain boat and heated at 250 °C for 2 h in a well-sealed tubular furnace with a heating rate of 5 °C min^{-1} under the Ar atmosphere. After cooling to room temperature, a large amount of DI water was used to remove solid white salt, and black Ni_7S_6 was successfully prepared. Finally, the Ni_7S_6 sample was washed with DI water and ethanol several times and dried in a vacuum oven for 24 h.

2.3. Synthesis of Ni_2P

Firstly, the pretreated Ni foam was placed at the bottom of the bottle and covered with 10 g $\text{Ni}(\text{NO}_3)_2 \cdot 6\text{H}_2\text{O}$. Then, the bottle was heated at 125 °C for 12 h in an oven. The resulting samples (NiNH) was rinsed with ethanol and dried for 24 h. Finally, the 1 g NaH_2PO_2 and prepared NiNH were placed upstream and downstream of a well-sealed tube furnace, respectively. Under the protection of Ar atmosphere, the sample was heated to 350 °C and reacted for 2 h with a heating rate of 2 °C min^{-1} . After natural cooling to ambient temperature, Ni_2P was yielded.

2.4. AEM water electrolyzer system assembly

The AEM water electrolyzer comprises the anode, cathode, gas diffusion layer, and anion exchange membrane (Fumasep FAA-3-50). The commercial Pt/C powder with the loading amount of 4 mg cm^{-2} was sprayed onto carbon paper as the anode electrocatalyst for comparison. The prepared $\text{Ni}_2\text{P}/\text{Ni}_7\text{S}_6$, Ni_7S_6 , and Ni foam were directly used as an anode to assemble the membrane electrode. Before use, the anion exchange membrane ($4 \times 4\text{ cm}^2$) was placed in 1 M KOH for more than 24 h, and the active working electrode area was 1 cm^2 in the single-cell. The alkaline electrolyte (1 M KOH) was recycled into the cathode and anode side through a self-priming pump from the electrolyte reservoir. The electrolyzer was heated by a heating rod, and an automatic temperature control device precisely controlled the temperature. When the temperature of the cell was stabilized, the performance of the cell was analyzed. In this paper, all electrochemical testing were performed on single-cell. The polarization curves of the AEM single-cell were evaluated at the range of 1.0–2.4 V with a scan rate of 2 mV s^{-1} by Gamry 3000 with an amplifier. The stability of AEM water electrolyzer systems was evaluated at the industrial scale current density of 1000 mA cm^{-2} . Electrochemical impedance spectroscopy (EIS) was carried out to measure the resistances of the single-cell. The corresponding energy efficiency was calculated based on the following formula:

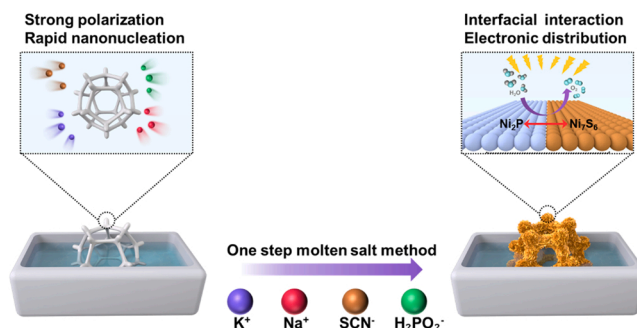
$$\eta = \frac{E_{\text{Output}}}{E_{\text{Input}}} = \frac{V_{\text{H}_2} \cdot H_0}{W_h} \times 100$$

Where, the total input electricity for hydrogen production was expressed as W_h . The H_0 was the calorific value of hydrogen ($10.8 \times 10^6\text{ J m}^{-3}$, lower heating value), and the V_{H_2} represented the total volume of producing hydrogen [23,24].

3. Results and discussion

3.1. Electrocatalyst preparation and characterization

As shown in Scheme 1, the porous $\text{Ni}_2\text{P}/\text{Ni}_7\text{S}_6$ nanosheets with maple leaf shape were first prepared on the surface of Ni foam by the one-step molten salt method. When the reaction temperature reaches the melting point of KSCN, the Ni atom from the Ni foam will coordinate with the S



Scheme 1. The schematic illustration of the preparation procedure for $\text{Ni}_2\text{P}/\text{Ni}_7\text{S}_6$ by the one-step molten salt method.

atom in SCN^- to form Ni_7S_6 with a high crystalline phase. With the help of the rapid ion migration in the molten salt system, Ni atoms from Ni foam can also combine with P atoms in the NaH_2PO_2 to synthesize the Ni_2P structure. Finally, the $\text{Ni}_2\text{P}/\text{Ni}_7\text{S}_6$ heterojunction interface with the rich porous structure was successfully constructed. And the pure Ni_7S_6 nanowires were successfully synthesized on Ni foam for comparison using a similar molten salt method, only not introducing NaH_2PO_2 . The optical photograph of the synthetic catalysts is shown in Fig. S2.

The scan electron microscopy (SEM) of Fig. 1a and Fig. S3 shows that the synthesized $\text{Ni}_2\text{P}/\text{Ni}_7\text{S}_6$ heterojunction catalyst is a maple leaf-shaped nanosheet structure grown uniformly on the smooth surface of Ni foam (Fig. S4), which can enlarge the catalytic surface area. The thickness of these nanosheets is about 40 nm and they are intertwined with each other. The ordered nanosheets coating on Ni foam have better mechanical strength than bare Ni foam, which will help the catalyst run stably under harsh test conditions (Fig. S5). By contrast, the Ni_7S_6 is a

simple nanowire structure with a diameter of about 250 nm (Fig. S6). The diameter of Ni_2P nanowire precursor is about 500 nm (Fig. S7).

The transmission electron microscopy (TEM) image of $\text{Ni}_2\text{P}/\text{Ni}_7\text{S}_6$ in Fig. 1b further highlights that heterojunction has regular nanosheet morphology. Notably, the black nanosheet bulk has plenty of white bright spots, implying the presence of pore structures. These abundant pores are favourable for maximizing the exposed electrocatalytic active sites and facilitating mass transportation in the reactions. Electron spin resonance (ESR) spectra is also employed to determine the formation of defects (Fig. S8). A broad signal can be assigned to the contribution from unpaired electrons, indicating vacancies (defects) exist in the $\text{Ni}_2\text{P}/\text{Ni}_7\text{S}_6$. The nitrogen absorption/desorption isotherm of $\text{Ni}_2\text{P}/\text{Ni}_7\text{S}_6$ (Fig. S9) reveals a Brunauer-Emmett-Teller (BET) surface area of $3.56 \text{ m}^2 \text{ g}^{-1}$. It seems a low BET surface area for $\text{Ni}_2\text{P}/\text{Ni}_7\text{S}_6$, while this is because that the mass of Ni foam is also considered in the measurements of BET surface area. And Barrett-Joyner-Halenda (BJH) pore-size

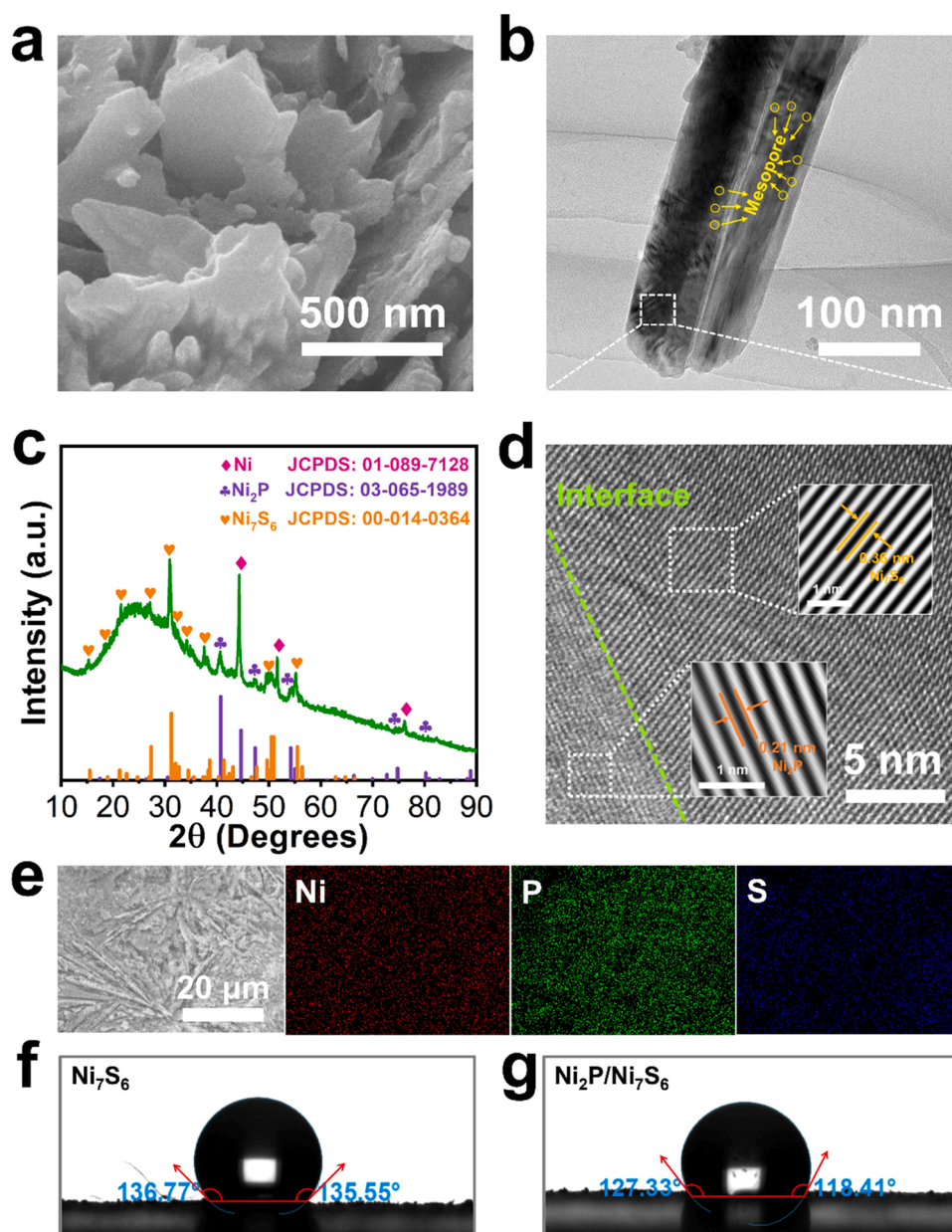


Fig. 1. (a) SEM photograph of the $\text{Ni}_2\text{P}/\text{Ni}_7\text{S}_6$ sample. (b) TEM photograph of the $\text{Ni}_2\text{P}/\text{Ni}_7\text{S}_6$ sample. (c) XRD pattern of $\text{Ni}_2\text{P}/\text{Ni}_7\text{S}_6$ samples. (d) HRTEM pattern of the $\text{Ni}_2\text{P}/\text{Ni}_7\text{S}_6$ sample. Insets of (d) are the corresponding FFT images. (e) EDS element mapping images of $\text{Ni}_2\text{P}/\text{Ni}_7\text{S}_6$. The solid-liquid contact angles of (f) Ni_7S_6 and (g) $\text{Ni}_2\text{P}/\text{Ni}_7\text{S}_6$.

distribution implies that $\text{Ni}_2\text{P}/\text{Ni}_7\text{S}_6$ has the mesoporous structures with average pore diameter of 23.52 nm. These pores may be related to the strong polarization etching of the molten salt in the synthesis process [25,26]. The X-ray diffraction (XRD) patterns in Fig. S10 and Fig. S11 are highly consistent with the PDF cards, which reveal that Ni_7S_6 and Ni_2P have almost pure-phase structure. After introducing the P element, the XRD pattern of $\text{Ni}_2\text{P}/\text{Ni}_7\text{S}_6$ (Fig. 1c) clearly shows three types of peaks corresponding to Ni (JCPDS No. 01–089–7128), Ni_2P (JCPDS No. 03–065–1989) and Ni_7S_6 (JCPDS No. 00–014–0364), respectively [27, 28]. The XRD results prove favorably that the heterojunction with high crystalline phase has been successfully fabricated. According to previous literature reports, this unique high-purity phase structure has good mechanical strength, which is conducive to long-time stable operation under industrial conditions [29]. The high-resolution TEM (HRTEM) image (Fig. 1d) exhibits continuous heterogeneous interface at the boundaries of these domains. And there are two kinds of clear lattice stripes, further confirming the successful preparation of heterojunction with a high crystalline phase. The lattice fringes treated by fast Fourier transformation (FFT) (inset of Fig. 1d) reveals two clearly lattice distances 0.36 and 0.21 nm, corresponding to the (100) plane of Ni_7S_6 and the (111) plane of Ni_2P , respectively. The elemental mapping images and energy dispersive spectroscopy (EDS) (Fig. 1e and Fig. S12) clarify the coexistence of Ni, S, and P in $\text{Ni}_2\text{P}/\text{Ni}_7\text{S}_6$. The solid-liquid contact angles of electrode material are further investigated in Fig. 1f and Fig. 1g. Obviously, the $\text{Ni}_2\text{P}/\text{Ni}_7\text{S}_6$ heterojunction nanosheet arrays have smaller contact angle values (118.41° and 127.33°) compared with Ni_7S_6 (135.55° and 136.77°). The change in contact angle is mainly attributed to the successful construction of heterojunctions with rich pore structures, which could optimize the local electron and mass transfer process, achieving efficient hydrogen production under industrial current density [10].

The surface electronic structure and chemical composition are analyzed detailedly by X-ray photoelectron spectroscopy (XPS). XPS survey spectra of Fig. 2a illustrates that the surface of $\text{Ni}_2\text{P}/\text{Ni}_7\text{S}_6$ is mainly composed of Ni, S and P elements. Other peaks attributed to reagents in the synthesis process have been labeled in detail. The metal nickel peaks (Ni^0) located at 852.7 eV are all observed in high-resolution XPS spectra of Ni 2p (Fig. 2b), which is mainly due to the Ni atoms on the surface of the Ni foam [30,31]. For the Ni 2p in $\text{Ni}_2\text{P}/\text{Ni}_7\text{S}_6$, two obvious peaks at the binding energies of 855.9 and 861.6 eV are well matched to the Ni 2p_{3/2} and one shakeup satellite peak. Moreover, the fitted peaks located at binding energies of 873.7 and 879.8 eV can be assigned to the Ni 2p_{1/2} with one broad satellite peak. Additionally, the peaks of the Ni 2p_{3/2} and Ni 2p_{1/2} in $\text{Ni}_2\text{P}/\text{Ni}_7\text{S}_6$ show a positive shift compared to that of Ni_7S_6 , while a negative shift compared to that of Ni_2P . The XPS results of Ni 2p strongly suggest the existence of electronic interactions between Ni_2P and Ni_7S_6 , leading to the redistribution of charge on their coupling interfaces [32,33]. The S 2p spectrum (Fig. 2c) of $\text{Ni}_2\text{P}/\text{Ni}_7\text{S}_6$ displays that the peak located at 161.9 eV is due to the Ni-S bonding, whereas the another one at 168.3 eV is associated with the S-O bonding originated from the solvent or oxidized S elements. In contrast, the Ni-S signal in the $\text{Ni}_2\text{P}/\text{Ni}_7\text{S}_6$ exhibits negative shift of about 0.45 eV, compared with that in the bare Ni_7S_6 . These observations indicate that Ni and S species in $\text{Ni}_2\text{P}/\text{Ni}_7\text{S}_6$ catalyst have a more partial positive charge (δ^+) and a negative charge (δ^-) than that of Ni_7S_6 catalyst after Ni_2P modification, respectively [34,50]. The P 2p spectra (Fig. 2d) of $\text{Ni}_2\text{P}/\text{Ni}_7\text{S}_6$ with the peaks located at a binding energy of 129.6 eV are attributed to the Ni-P bonding. Moreover, there is a signal peak of the P-O bonding situated at 132.9 eV, suggesting surface oxidation under ambient conditions. Due to the weak electronegativity of P element, the chemical state of Ni-P bonding in $\text{Ni}_2\text{P}/\text{Ni}_7\text{S}_6$ has not changed significantly compared with that of Ni_2P . But the P-O peak of $\text{Ni}_2\text{P}/\text{Ni}_7\text{S}_6$ has a

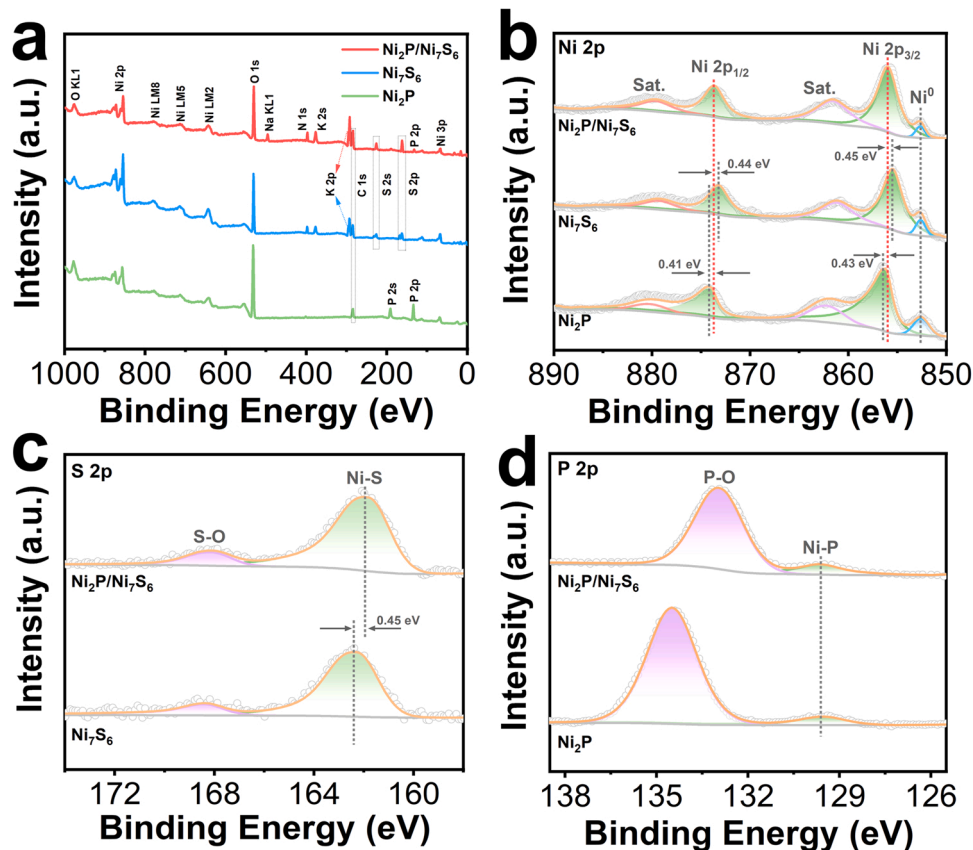


Fig. 2. (a) XPS survey spectrum of the $\text{Ni}_2\text{P}/\text{Ni}_7\text{S}_6$, Ni_7S_6 and Ni_2P samples. (b) The Ni 2p high-resolution XPS spectrum of the $\text{Ni}_2\text{P}/\text{Ni}_7\text{S}_6$, Ni_7S_6 and Ni_2P samples. (c) The S 2p high-resolution XPS spectra of the $\text{Ni}_2\text{P}/\text{Ni}_7\text{S}_6$ and Ni_7S_6 samples. (d) The P 2p high-resolution XPS spectra of the $\text{Ni}_2\text{P}/\text{Ni}_7\text{S}_6$ and Ni_2P samples.

negative shift compared to that of Ni₂P, revealing that the charge redistribution happens due to the strong interaction at the interface of the Ni₂P and Ni₇S₆ in Ni₂P/Ni₇S₆ [35].

3.2. Electrocatalytic performance

All the OER electrochemical measurement was carried out in the standard three-electrode system, in which a cartoon of the setup was presented in Fig. 3a. Firstly, the OER performances of Ni₂P/Ni₇S₆ and other referential catalysts were evaluated by the linear sweep voltammetry (LSV) with iR correction. Similar to previous literature reports, Zhao et al. have reported the oxidation peak of nickel species in Ni(OH)₂ during OER test. And the catalyst inhibits the oxidation peak of nickel most obviously after doping Fe element [36]. Noticeably, the oxidation peak (Fig. S13) of nickel species in the Ni₂P/Ni₇S₆ is greatly suppressed compared with other comparison samples. The absence of the oxidation peak may be due to promoting charge transfer between Ni and P atoms and raising the valence state of the Ni atom after constructing the heterojunction interface, which is consistent with the XPS analysis results [37]. Heterojunction structure could greatly reduce energy consumption by inhibiting oxidation peak, promoting hydrogen economy.

Fig. 3a exhibits that Ni₂P/Ni₇S₆ with excellent OER performance only requires a lower overpotential of 257, 304 and 330 mV to drive the current density of 100, 500 and 1000 mA cm⁻², which is better than those of Ni₂P (η_{100} = 284 mV, η_{500} = 331 mV and η_{1000} = 370 mV), Ni₇S₆ (η_{100} = 306 mV, η_{500} = 366 mV and η_{1000} = 403 mV) and Ni foam (η_{100} = 359 mV, η_{500} = 429 mV and η_{1000} = 480 mV). The above results show that the significant improvement for OER performance is mainly attributed to the synergistic effect of the high crystalline heterogeneous interface and the unique maple leaf-shaped nanosheet structure with rich defect sites. Fig. 3b visually displays the OER overpotential comparison between Ni₂P/Ni₇S₆ and other samples at different current densities (100, 500 and 1000 mA cm⁻²). Its performance remains unchanged after multiple folds (Fig. S14), showing excellent mechanical strength. As depicted in Fig. 3c, the Tafel slope of 69 mV dec⁻¹ for Ni₂P/Ni₇S₆ is much smaller than that of Ni₂P (76 mV dec⁻¹), Ni₇S₆ (89 mV dec⁻¹) and Ni foam (104 mV dec⁻¹), suggesting more excellent reaction kinetics achieved by regulating electronic structure in heterojunction Ni₂P/Ni₇S₆ electrode. In order to deeply understand the reasons for OER performance improvement, the electrochemical double layer capacitances (C_{dl}) obtained from the CV test are accustomed to calculating the electrochemical surface area (ECSA) of Ni₂P/Ni₇S₆, Ni₂P, Ni₇S₆ and Ni

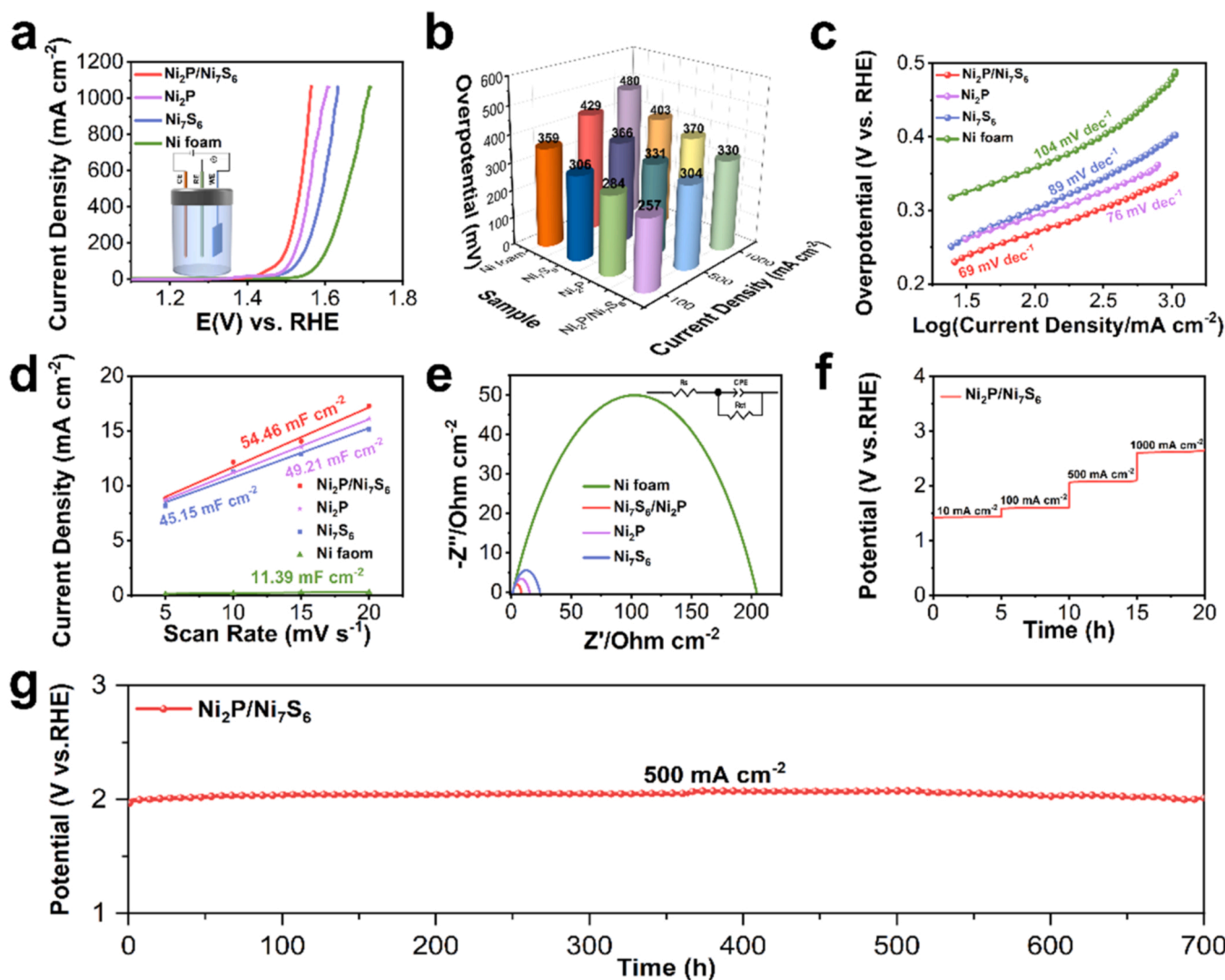


Fig. 3. (a) OER polarization curves of Ni₂P/Ni₇S₆, Ni₂P, Ni₇S₆ and Ni foam with a scan rate of 2 mV s⁻¹ in 1 M KOH, inset: A cartoon of the standard three-electrode system. (b) The comparison of overpotential at 100 500 and 1000 mA cm⁻² for Ni₂P/Ni₇S₆ and other references. (c) The corresponding Tafel plots. (d) Double layer capacitor of the as-prepared catalysts. (e) Electrochemical impedance spectra (EIS) of Ni₂P/Ni₇S₆, Ni₂P, Ni₇S₆ and Ni foam. (f) Stability tests at 10, 100, 500 and 1000 mA cm⁻² for 20 h. (g) Chronopotentiometry curves of the Ni₂P/Ni₇S₆ in 1 M KOH at a current density of 1000 mA cm⁻² for 700 h.

foam. Figs. 3d and S15 exhibit that the C_{dl} value of Ni₂P/Ni₇S₆, Ni₂P, Ni₇S₆ and Ni foam are 54.46, 49.21, 45.15 and 11.39 mF cm⁻², and the corresponding ECSAs are calculated to be 1361.51, 1230.25, 1128.75 and 284.75 cm², respectively, as listed in Table S1. After ECSA normalization of LSV curves (Fig. S16), the high crystalline phase heterojunction Ni₂P/Ni₇S₆ still has lower overpotential and better activity than Ni₂P, Ni₇S₆ and Ni foam, which also confirms that the enhancement of intrinsic activity is due to the synergetic effect between Ni₂P and Ni₇S₆. Similarly, Ni₂P/Ni₇S₆ sample shows a turnover frequency (TOF) value ratio of 5 times higher than Ni₇S₆ in Fig. S17, which further emphasizes that Ni₂P/Ni₇S₆ with abundant active sites has excellent OER intrinsic activity. In order to better investigate the charge transfer of catalysts, electrochemical impedance spectroscopy (EIS) is performed to study the conductivity of the electrode towards OER. As revealed in Fig. 3e, Ni₂P/Ni₇S₆ delivers a much lower charge-transfer resistance (R_{ct} , 7.39 Ω) than Ni₂P (14.21 Ω), Ni₇S₆ (22.82 Ω) and Ni foam (203.22 Ω), demonstrating that the Ni₂P/Ni₇S₆ possesses a faster charge transfer kinetics and superior conductivity during OER process corresponding to the Tafel results. The above analysis suggests that the successful construction of the heterojunction interface will significantly improve the conductivity and OER performance [38–40].

From the practical application perspective, the stability of the catalyst, especially the long-term stability under high current density, is an essential criterion for evaluating the OER electrocatalyst. In order to meet the intermittent operation characteristics of renewable energy, the stability test of Ni₂P/Ni₇S₆ under different current densities (Fig. 3f) is carried out to exhibit good operability. Moreover, the ultra-long chronopotentiometry test (Fig. 3g) also displays that the Ni₂P/Ni₇S₆ could operate stably for 700 h at the industrial current density of 500 mA cm⁻² without noticeable performance degradation. Although some heterostructure catalysts for OER have been reported recently. For example, Wang et al. have documented the synthesis of Ni₂P/NiMoP heterostructure through a simple hydrothermal and phosphorization method [14]. Feng et al. demonstrate the design and construction of hierarchical FeP/Ni₂P hybrid hollow nanospindles (HNSSs) as an active and stable electrocatalyst for the oxygen evolution [22]. However, these heterostructures synthesized by complicated steps are difficult to run stably at high oxidation potential for a long time. By contrast, the OER performance of Ni₂P/Ni₇S₆, including activity and stability, has surpassed most of the transition metal catalysts reported, especially in industrial-scale operating conditions (Table S2). The excellent performance of Ni₂P/Ni₇S₆ is not only attributed to the good mechanical strength and fast mass transfer ability of its maple leaf porous heterojunction, but also related to the adjustable electronic structure and superior conductivity at the heterojunction interface with high crystalline phase [41,42]. These advantages enable the catalyst to meet harsh industrial test conditions, presenting auspicious industrial application potentiality. After the stability test, the maple leaf nanosheets structure remained (Fig. S18). But its surface was coated with thinner nanosheets caused by long-term high current conditions. Reconstructed hydroxide nanosheets will help to reduce the loss of elements and play a positive role in prolonging the life of electrocatalysts [43]. The XPS survey spectra (Fig. S19a) shows that the peak intensities of S and P elements decrease after the stability test, suggesting that there is a certain loss phenomenon. As depicted in Fig. S19b, the Ni 2p_{3/2} peak located at 856.6 eV exhibits positive shift of about 0.53 eV after stability test. This phenomenon is mainly due to the long-time stability test under high oxidation environment, rising the valence state of Ni element [44,45]. After stability test, the P and S elements have obvious loss phenomenon after stability in XPS survey spectrum. The surface S and P atoms are leached leading to the low intensity in S 2p and P 2p spectrum (Fig. S19c, d). Combined with the above results, it can be concluded that the surface hydroxide reconstruction account for the long-term stability, but also leads to the formation of vertically thin nanosheet morphology [46,47]. We believe that the loss of P and S elements is just a surface behavior. The internal high-crystal structure has good skeleton support

and mechanical strength, ensuring that the overall catalyst can stably operate under harsh environments for long time.

3.3. Lab-scaled AEMWE single-cell testing

As for commercial applications, the anion exchange membrane water electrolysis (AEMWE) stack system is presented in Fig. 4a, including electrolytic system, water/gas loop systems, heating system, and control system. A single-cell AEMWE with an active area of 1 cm² by coupling (Pt/C) cathode with the Ni₂P/Ni₇S₆ (Ni₂P/Ni₇S₆/(Pt/C)), Ni₂P (Ni₂P/(Pt/C)), Ni₇S₆ (Ni₇S₆/(Pt/C)) and Ni foam (Ni foam/(Pt/C)) was assembled in Fig. 4b and Fig. S20 to measure the AEMWE performance.

In order to systematically evaluate the AEMWE performance, we built a set of AEM test system in the laboratory equipped with an automatic temperature control system and electrolyte circulation system (Fig. S21). The LSV polarization curves of the AEMWE single-cell (Fig. 4c) reveal that the Ni₂P/Ni₇S₆/(Pt/C) exhibits good performance (203.9 mA cm⁻²), in comparison with that of Ni₂P/(Pt/C) (116.51 mA cm⁻²), Ni₇S₆/(Pt/C) (70.89 mA cm⁻²) and Ni foam/(Pt/C) (23.94 mA cm⁻²) at 2.0 V under the conventional operating conditions (1 M KOH solution at 25 °C). Electrochemical impedance spectroscopy (EIS) is performed at the cell voltage of about 1.7 V to analyze the differences in the performances (Fig. 4d). According to the equivalent circuit model in Fig. S22a, the single-cell resistance of AEMWE can be used to quantify the EIS measurements. The impact of the individual impedances in the Nyquist plot can be divided into two parts (Fig. S22b): bulk (R_b) and charge transfer (R_{ct}) [48,49]. Interestingly, R_b and R_{ct} values of Ni₂P/Ni₇S₆/(Pt/C) are significantly lower than those of Ni₂P/(Pt/C), Ni₇S₆/(Pt/C) and Ni foam/(Pt/C) in Table S3. Moreover, Ni₂P/Ni₇S₆/(Pt/C) exhibits excellent current density at different cell voltages compared with Ni₂P/(Pt/C), Ni₇S₆/(Pt/C) and Ni foam/(Pt/C) (Fig. 4e). This further proves that the heterojunction with high crystalline phase and superior conductivity plays an active role in efficient AEM water electrolysis. Considering the industrial operation, the catalytic performance of the Ni₂P/Ni₇S₆/(Pt/C) is evaluated at different temperatures. The Ni₂P/Ni₇S₆/(Pt/C) at 75 °C exhibits the most outstanding cell performance (1.88 V@1000 mA cm⁻²) compared with 65 °C (1.94 V@1000 mA cm⁻²), 55 °C (1.99 V@1000 mA cm⁻²) and 45 °C (2.05 V@1000 mA cm⁻²) in Fig. 4f. Then, we analyze the cell resistance at different temperatures to explain the reason for the performance improvement (Fig. 4g and Table S4). The decreasing R_b value with the temperature increase may be mainly related to the conductivity of the ionomer and anion [49]. At the same time, the decreasing R_{ct} value also shows that the temperature increase will accelerate the kinetics, speed up the electron transmission, and thus improve the AEMWE performance. Compared with the AEMWE performance reported to date, our cell (Ni₂P/Ni₇S₆/(Pt/C)) also has surpassed most single-cell AEM electrolytic cells, displaying extraordinary performance (Fig. 4h and Table S5). The AEMWE (Ni₂P/Ni₇S₆/(Pt/C)) can operate stably with a degradation rate of 3.2 mV h⁻¹ at 1000 mA cm⁻² in 1 M KOH (25 °C) for 100 h (Fig. S23). Furthermore, the amount of hydrogen produced from the single cell is 13 ml min⁻¹ by a mass flow meter at 25 °C. The average energy efficiency is about 63 %, which was maintained for 100 h at a constant current density of 1000 mA cm⁻² (Fig. S24). When the operating temperature is 75 °C, the cell (Ni₂P/Ni₇S₆/(Pt/C)) is conducted at 1000 mA cm⁻² in 1 M KOH for 140 h with a lower degradation rate of 1.9 mV h⁻¹ (Fig. 4i). During a 140 h test at a higher temperature of 75 °C, an energy efficiency is maintained over 72 % (Fig. S25), and the rate of hydrogen production is as high as 15 ml min⁻¹. As the temperature of the test system increases, the hydrogen production rate and energy efficiency are greatly improved. This finding enlightens us that moderately increasing the operating temperature will contribute to improving hydrogen production efficiency, providing a broad application prospect for industrial hydrogen production.

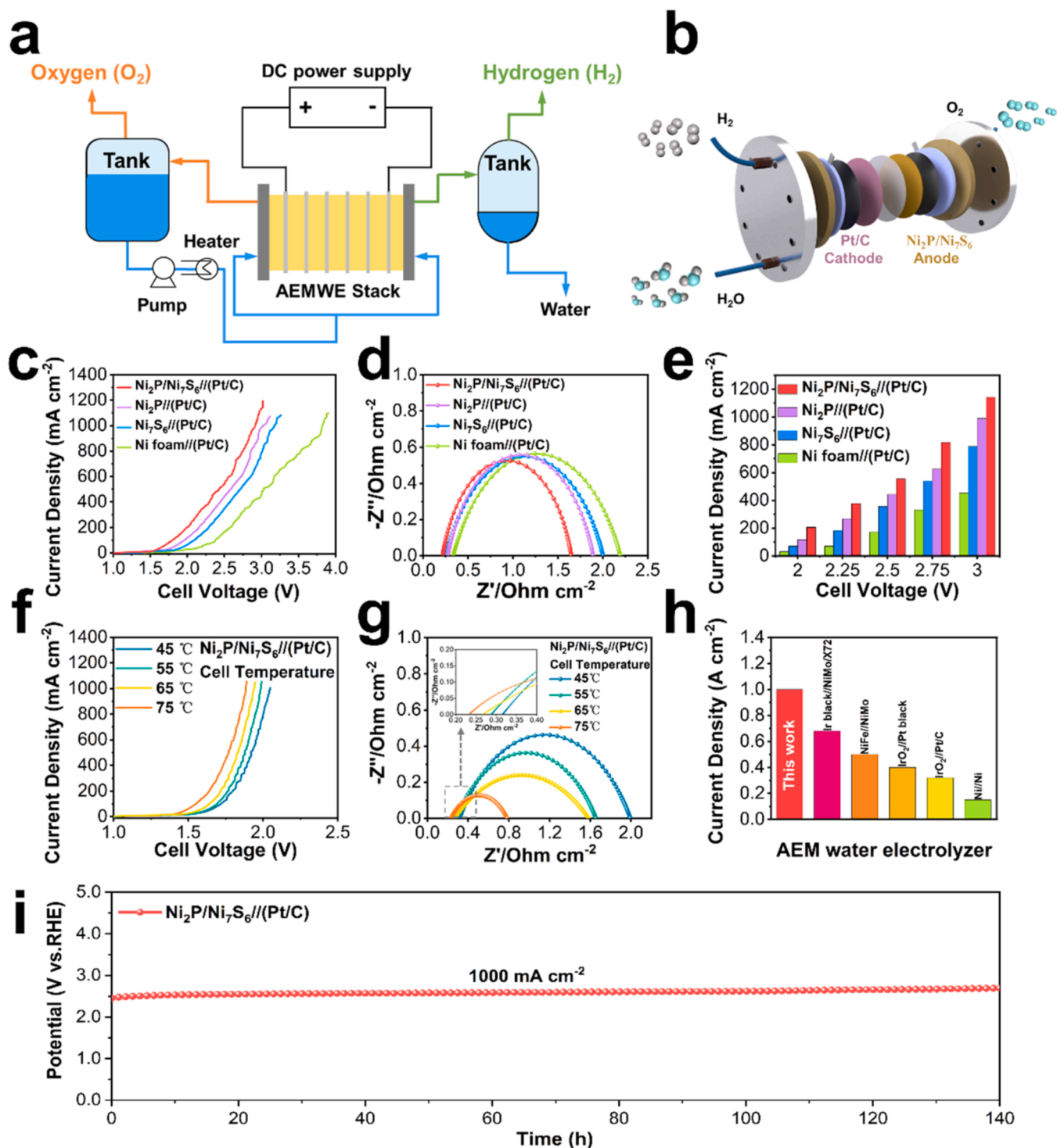


Fig. 4. Performances of the designed AEM water electrolyzer. (a) Schematic diagram of the AEMWE stack system. (b) Schematic of the single-cell AEMWE stack. (c) Polarization curves of AEM water electrolyzer with Ni₂P/Ni₇S₆, Ni₇S₆ and Ni foam as the anode, and Pt/C as the cathode in 1 M KOH at 25 °C. (d) Electrochemical impedance spectra (EIS) of the as-prepared catalysts at the cell voltage of about 1.7 V. (e) Current density at various cell voltages for Ni₂P/Ni₇S₆ // (Pt/C), Ni₇S₆ // (Pt/C), and Ni foam // (Pt/C) cells. (f) Polarization curves comparison of Ni₂P/Ni₇S₆ // (Pt/C) at different temperature. (g) Electrochemical impedance spectra (EIS) of at different temperature. (h) Comparison the current density of AEM water electrolyzer for the Ni₂P/Ni₇S₆ // (Pt/C) cell and the reported AEM water electrolyzer cells at the cell voltage of about 1.88 V. (i) Durability cell voltage-time plots for the AEM water electrolyzer (Ni₂P/Ni₇S₆ // (Pt/C) cell) at a constant current density of 1000 mA cm⁻² for 140 h in 1 M KOH at 75 °C.

3.4. Theoretical calculation

Density functional theory (DFT) calculation is implemented to explain the unique advantages of Ni₂P/Ni₇S₆ heterojunction and reveal the intrinsic cause of OER performance improvement. According to

previous literature, Ni₂P (001) and Ni₇S₆ (100) planes are selected as stable crystal planes to construct the heterojunction [50,51]. And the optimized Ni₂P/Ni₇S₆ heterojunction model is shown in Fig. 5a. As analyzed from the density of state (DOS) (Fig. 5b), the electronic states of the Ni₂P/Ni₇S₆ heterojunction have a higher DOS near the Fermi level

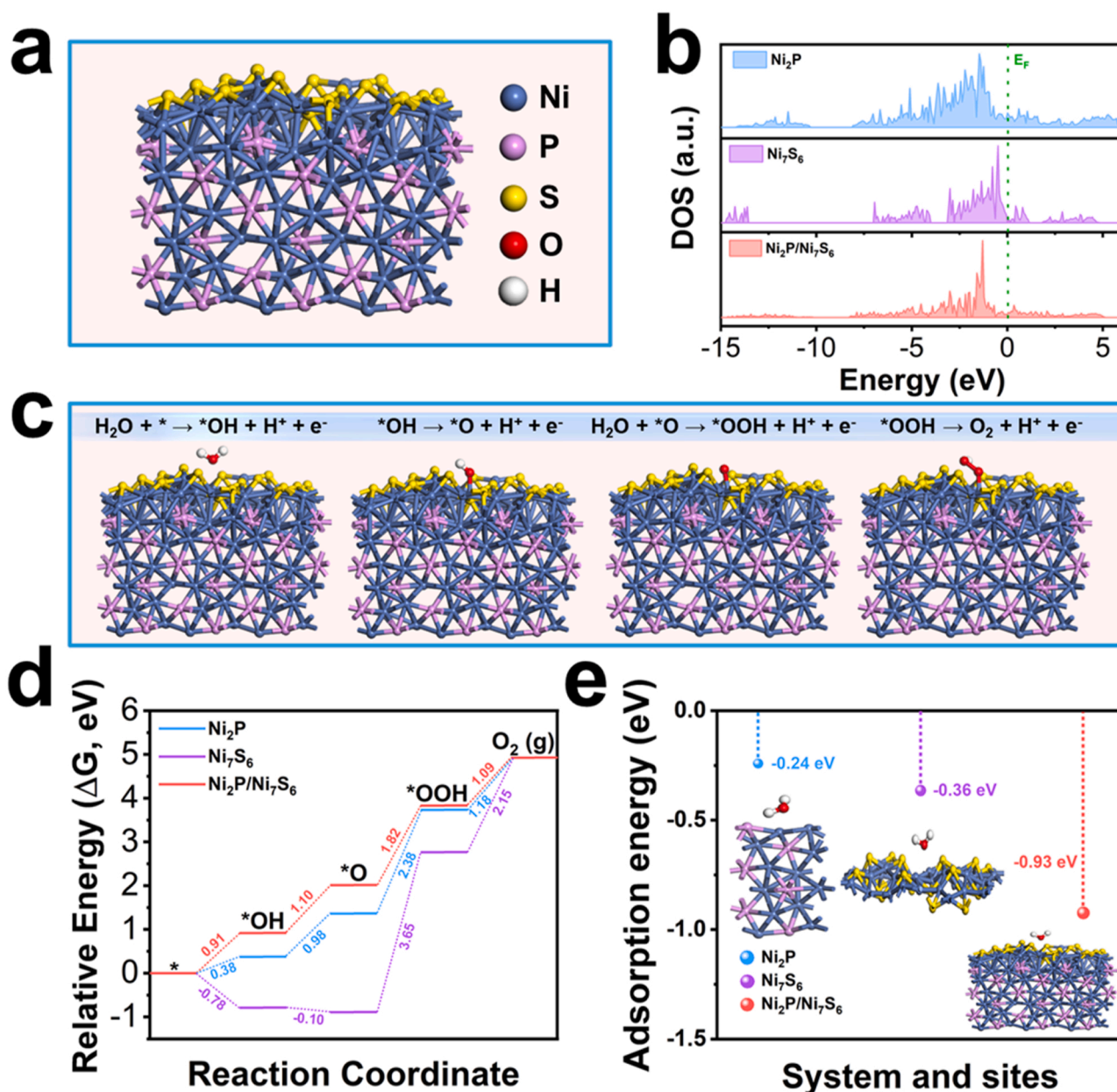


Fig. 5. (a) The atomic structure of the interface system built by the Ni_2P and Ni_7S_6 . (b) The DOSs of Ni_2P , Ni_7S_6 , and $\text{Ni}_2\text{P}/\text{Ni}_7\text{S}_6$. (c) The illustration of four elementary steps of OER occurred on $\text{Ni}_2\text{P}/\text{Ni}_7\text{S}_6$. (d) The free-energy diagrams of the OER pathway for Ni_2P , Ni_7S_6 , and $\text{Ni}_2\text{P}/\text{Ni}_7\text{S}_6$. (e) The adsorption energies of H_2O on the surface of Ni_2P , Ni_7S_6 , and $\text{Ni}_2\text{P}/\text{Ni}_7\text{S}_6$.

relative to those of pristine Ni_7S_6 , leading to enhanced electrical conductivity due to decreased localization of electrons [50,52]. The electron density of the $\text{Ni}_2\text{P}/\text{Ni}_7\text{S}_6$ interface (Fig. S26) further proves that the electronic structure has been dramatically redistributed. This may be due to the fact that the highly electronegative P and S atoms jointly attract electrons on the Ni atoms for superior conductivity, which is consistent with the results of XPS analysis. Moreover, the heterojunction may also help to regulate the binding interaction with the OER intermediate on the catalyst surface. The optimized models of four-step intermediates (Slab, $*OH$, $*O$, and $*OOH$) on the $\text{Ni}_2\text{P}/\text{Ni}_7\text{S}_6$ heterojunction are illustrated in Fig. 5c. In contrast, the Ni site is also adsorbed by the OER intermediate in Ni_7S_6 and Ni_2P model, and the optimized configuration is shown in Fig. S27 and Fig. S28. As displayed in Fig. 5d, the formation step of $*OOH$ is the rate-determining step (RDS) for $\text{Ni}_2\text{P}/\text{Ni}_7\text{S}_6$, Ni_7S_6 and Ni_2P . The Gibbs free energy change (ΔG) of the RDS for $\text{Ni}_2\text{P}/\text{Ni}_7\text{S}_6$ is calculated to be 1.82 eV, which is significantly

lower than that of Ni_2P (2.38 eV) and Ni_7S_6 (3.65 eV). Thanks to the distribution of electrons at the heterojunction interface, $\text{Ni}_2\text{P}/\text{Ni}_7\text{S}_6$ electrocatalyst will greatly reduce the energy barrier of RDS, thus offering excellent OER activity. Furthermore, the adsorption energy (Fig. 5e) of water molecules (H_2O) on the catalyst surface will also be viewed as an essential index to evaluate the OER performance [21,53]. The chemisorption energy of water is -0.24, -0.36 and -0.93 eV for Ni_2P , Ni_7S_6 and $\text{Ni}_2\text{P}/\text{Ni}_7\text{S}_6$, respectively, which indicates that H_2O molecules have better binding force on the catalytic surface and promote the adsorption of oxygen-containing intermediates on $\text{Ni}_2\text{P}/\text{Ni}_7\text{S}_6$ heterojunction. The above theoretical simulation results demonstrate that constructing a heterojunction can effectively enhance the overall conductivity by adjusting the two-phase electronic structure and markedly reduce the reaction energy barrier, achieving splendid OER performance.

4. Conclusions

In summary, the maple leaf-shaped porous heterojunction of Ni₂P/Ni₇S₆ has been constructed on Ni foam by the one-step molten salt method toward industrial oxygen evolution. It is revealed that the porous high crystalline phase structure not only exposes more active sites but also exhibits superior conductivity. Moreover, the electron redistribution around the heterointerface promotes the adsorption of H₂O molecules as well as optimizing the binding energy of *OOH intermediates on the catalytic Ni sites. The obtained Ni₂P/Ni₇S₆ heterostructure shows outstanding OER performance with an ultralow overpotentials of 304 and 330 mV, reaching an industrial-level current density of 500 and 1000 mA cm⁻² in 1 M KOH, respectively. For large-scale industrial applications, the single-cell AEM electrolyzer (Ni₂P/Ni₇S₆/(Pt/C)) demonstrates remarkable performance (1000 mA cm⁻² at 1.88 V_{cell}) and energy efficiency (72 % at 1000 mA cm⁻²) during a 140-h practical test. This current work opens new insights for developing highly active and stable electrocatalysts to achieve large-scale water splitting.

CRediT authorship contribution statement

Fu-Li Wang: Data curation, Writing - original draft, Formal analysis, Investigation, Writing - review & editing. **Na Xu:** Writing - original draft, Conceptualization, Formal analysis, Writing - review & editing. **Cheng-Jie Yu:** Writing - review & editing, Formal analysis. **Jing-Yi Xie:** Writing - original draft, Formal analysis, Methodology. **Bin Dong:** Formal analysis, Investigation, Resources, Writing - original draft, Funding acquisition, Project administration, Writing - review & editing. **Xin-Yu Zhang:** Writing - original draft, Formal analysis. **Yi-Wen Dong:** Writing - review & editing, Formal analysis. **Yu-Lu Zhou:** Writing - original draft, Writing - review & editing. **Yong-Ming Chai:** Funding acquisition, Conceptualization, Investigation, Resources, Formal analysis, Supervision, Writing - review & editing.

Declaration of Competing Interest

The authors declare that they have no known competing financial interests or personal relationships that could have appeared to influence the work reported in this paper.

Data Availability

Data will be made available on request.

Acknowledgments

This work is financially supported by National Natural Science Foundation of China (52274308 and 52174283).

Appendix A. Supporting information

Supplementary data associated with this article can be found in the online version at [doi:10.1016/j.apcatb.2023.122633](https://doi.org/10.1016/j.apcatb.2023.122633).

References

- [1] K. Guo, Y. Wang, J. Huang, M. Lu, H. Li, Y. Peng, P. Xi, H. Zhang, J. Huang, S. Lu, C. Xu, In situ activated Co_{3-x}Ni_xO₄ as a highly active and ultrastable electrocatalyst for hydrogen generation, *ACS Catal.* 11 (2021) 8174–8182, <https://doi.org/10.1021/acscatal.1c01607>.
- [2] Y. Sun, H. Liao, J. Wang, B. Chen, S. Sun, S.J.H. Ong, S. Xi, C. Diao, Y. Du, J. O. Wang, M.B.H. Breese, S. Li, H. Zhang, Z.J. Xu, Covalency competition dominates the water oxidation structure–activity relationship on spinel oxides, *Nat. Catal.* 2 (2020) 554–563, <https://doi.org/10.1038/s41929-020-0465-6>.
- [3] Y.N. Zhou, W.L. Yu, Y.N. Cao, J. Zhao, B. Dong, Y. Ma, F.L. Wang, R.Y. Fan, Y. L. Zhou, Y.M. Chai, S-doped nickel-iron hydroxides synthesized by room-temperature electrochemical activation for efficient oxygen evolution, *Appl. Catal. B Environ.* 292 (2021), 120150, <https://doi.org/10.1016/j.apcatb.2021.120150>.
- [4] X. Li, Q. Hu, H. Yang, T. Ma, X. Chai, C. He, Bimetallic two-dimensional materials for electrocatalytic oxygen evolution, *Chin. Chem. Lett.* 33 (2022) 3657–3671, <https://doi.org/10.1016/j.ccl.2021.12.001>.
- [5] J. Li, Oxygen evolution reaction in energy conversion and storage: design strategies under and beyond the energy scaling relationship, *Nano-Micro Lett.* 14 (2022) 112, <https://doi.org/10.1007/s40820-022-00857-x>.
- [6] F.G. Wang, X. Liu, Q.X. Lv, B. Liu, Y.M. Chai, B. Dong, Transition metal boride-based materials for electrocatalytic water splitting, *Chin. J. Struct. Chem.* 41 (2022) 2209008–2209044, <https://doi.org/10.14102/j.cnki.0254-5861.2022-0117>.
- [7] W. Wang, Z. Wang, Y. Hu, Y. Liu, S. Chen, A potential-driven switch of activity promotion mode for the oxygen evolution reaction at Co₃O₄/NiO_xH_y interface, *eScience* 2 (2022) 438–444, <https://doi.org/10.1016/j.esci.2022.04.004>.
- [8] R.A. Krivina, G.A. Lindquist, S.R. Beaudoin, T.N. Stovall, W.L. Thompson, L. P. Twilight, D. Marsh, J. Grzyb, K. Fabrizio, J.E. Hutchison, S.W. Boettcher, Anode catalysts in anion-exchange-membrane electrolysis without supporting electrolyte: conductivity, dynamics, and ionomer degradation, *Adv. Mater.* 34 (2022) 2203033, <https://doi.org/10.1002/adma.202203033>.
- [9] K. Ayers, N. Danilovic, R. Ouimet, M. Carmo, B. Pivovar, M. Bornstein, Perspectives on low-temperature electrolysis and potential for renewable hydrogen at scale, *Annu. Rev. Chem. Biomol. Eng.* 10 (2019) 219–239, <https://doi.org/10.1146/annurev-chembioeng-060718-030241>.
- [10] Q. Wen, K. Yang, D. Huang, G. Cheng, X. Ai, Y. Liu, J. Fang, H. Li, L. Yu, T. Zhai, Schottky heterojunction nanosheet array achieving high-current-density oxygen evolution for industrial water splitting electrolyzers, *Adv. Energy Mater.* 11 (2021) 2102353, <https://doi.org/10.1002/aenm.202102353>.
- [11] D. Chen, R. Yu, D. Wu, H. Zhao, P. Wang, J. Zhu, P. Ji, Z. Pu, L. Chen, J. Yu, S. Mu, Anion-modulated molybdenum oxide enclosed ruthenium nano-capsules with almost the same water splitting capability in acidic and alkaline media, *Nano Energy* 100 (2022), 107445, <https://doi.org/10.1016/j.nanoen.2022.107445>.
- [12] R. Yang, X. Shi, Y. Wang, J. Jin, H. Liu, J. Yin, Y.Q. Zhao, P. Xi, Ruthenium-modified porous NiCo₂O₄ nanosheets boost overall water splitting in alkaline solution, *Chin. Chem. Lett.* 33 (2022) 4930–4935, <https://doi.org/10.1016/j.ccl.2021.12.058>.
- [13] X.P. Li, C. Huang, W.K. Han, T. Ouyang, Z.Q. Liu, Transition metal-based electrocatalysts for overall water splitting, *Chin. Chem. Lett.* 32 (2021) 2597–2616, <https://doi.org/10.1016/j.ccl.2021.01.047>.
- [14] T. Wang, X. Cao, L. Jiao, Ni₂P/NiMoP heterostructure as a bifunctional electrocatalyst for energy-saving hydrogen production, *eScience* 1 (2021) 69–74, <https://doi.org/10.1016/j.esci.2021.09.002>.
- [15] L.C. Xia, L.L. Bo, W.P. Shi, Y.N. Zhang, Y.X. Shen, X.C. Ji, X.L. Guan, Y.X. Wang, J. H. Tong, Defect and interface engineering of templated synthesis of hollow porous Co₃O₄/CoMoO₄ with highly enhanced electrocatalytic activity for oxygen evolution reaction, *Chem. Eng. J.* 452 (2023), 139250, <https://doi.org/10.1016/j.cej.2022.139250>.
- [16] L.L. Feng, G. Yu, Y. Wu, G.D. Li, H. Li, Y. Sun, T. Asefa, W. Chen, X. Zou, High-index faceted Ni₃S₂ nanosheet arrays as highly active and ultrastable electrocatalysts for water splitting, *J. Am. Chem. Soc.* 137 (2015) 14023–14026, <https://doi.org/10.1021/jacs.5b08186>.
- [17] P. Wang, Y. Luo, G. Zhang, Z. Chen, H. Ranganathan, S. Sun, Z. Shi, Interface engineering of Ni₃S₂@MnO_xH_y nanorods to efficiently enhance overall-water-splitting activity and stability, *Nano-Micro Lett.* 14 (2022) 120, <https://doi.org/10.1007/s40820-022-00860-2>.
- [18] F. Zeng, M. Yu, W. Cheng, W. He, Y. Pan, Y. Qu, C. Yuan, Tunable surface selenization on MoO₂-based carbon substrate for notably enhanced sodium-ion storage properties, *Small* 16 (2020) 2001905, <https://doi.org/10.1002/sml.2020019>.
- [19] H. Zhang, B. Xi, Y. Gu, W. Chen, S. Xiong, Interface engineering and heterometal doping Mo-NiS/Ni(OH)₂ for overall water splitting, *Nano Res* 14 (2021) 3466–3473, <https://doi.org/10.1007/s12274-021-3557-y>.
- [20] J.F. Qin, M. Yang, T.S. Chen, B. Dong, S. Hou, X. Ma, Y.N. Zhou, X.L. Yang, J. Nan, Y.M. Chai, Ternary metal sulfides MoCoNiS derived from metal organic frameworks for efficient oxygen evolution, *Inter. J. Hydrog. Energy* 45 (2020) 2745–2753, <https://doi.org/10.1016/j.ijhydene.2019.11.156>.
- [21] T. Li, T. Lu, Y. Li, J. Yin, Y. Tang, M. Zhang, H. Pang, L. Xu, J. Yang, Y. Zhang, Interfacial engineering-induced electronic regulation drastically enhances the electrocatalytic oxygen evolution: immobilization of Janus-structured NiS/NiO nanoparticles onto carbon nanotubes/nanofiber-integrated superstructures, *Chem. Eng. J.* 428 (2022), 131094, <https://doi.org/10.1016/j.cej.2021.131094>.
- [22] Y. Feng, C. Xu, E. Hu, B. Xia, J. Ning, C. Zheng, Y. Zhong, Z. Zhang, Y. Hu, Construction of hierarchical FeP/Ni₂P hollow nanospindles for efficient oxygen evolution, *J. Mater. Chem. A* 6 (2018) 14103–14111, <https://doi.org/10.1039/C8TA03933J>.
- [23] J. Lee, H. Jung, Y.S. Park, S. Woo, N. Kwon, Y. Xing, S.H. Oh, S.M. Choi, J.W. Han, B. Lim, Corrosion-engineered bimetallic oxide electrode as anode for high-efficiency anion exchange membrane water electrolyzer, *Chem. Eng. J.* 420 (2021), 127670, <https://doi.org/10.1016/j.cej.2020.127670>.
- [24] J. Lee, H. Jung, Y.S. Park, S. Woo, J. Yang, M.J. Jang, J. Jeong, N. Kwon, B. Lim, J. W. Han, S.M. Choi, High-efficiency anion-exchange membrane water electrolyzer enabled by ternary layered double hydroxide anode, *Small* 17 (2021) 2100639, <https://doi.org/10.1002/sml.202100639>.
- [25] W.K. Gao, M. Yang, J.Q. Chi, X.Y. Zhang, J.Y. Xie, B.Y. Guo, L. Wang, Y.M. Chai, B. Dong, In situ construction of surface defects of carbon-doped ternary cobalt-

- nickel-iron phosphides nanocubes for efficient overall water splitting, *Sci. China Mater.* 62 (2019) 1285–1296, <https://doi.org/10.1007/s40843-019-9434-7>.
- [26] F.L. Wang, X.Y. Li, Y.W. Dong, J. Nan, Y.M. Sun, H.B. Yu, X.Y. Zhang, B. Dong, Y. M. Chai, Strong ion interaction inducing ultrahigh activity of NiCoP nanowires for overall water splitting at large current density, *Appl. Surf. Sci.* 589 (2022), 152837, <https://doi.org/10.1016/j.apsusc.2022.152837>.
- [27] L. An, J. Feng, Y. Zhang, R. Wang, H. Liu, H. Liu, G.C. Wang, F. Cheng, P. Xi, Epitaxial heterogeneous interfaces on N-NiMoO₄/NiS₂ nanowires/nanosheets to boost hydrogen and oxygen production for overall water splitting, *Adv. Funct. Mater.* 29 (2019) 1805298, <https://doi.org/10.1002/adfm.201805298>.
- [28] S. Rundqvist, M. Yhland, R. Dahlbom, J. Sjövall, O. Theander, H. Flood, X-ray investigations of Mn₃P, Mn₂P, and Ni₂P, *Acta Chem. Scand.* 16 (1962) 992–998, <https://doi.org/10.3891/acta.chem.scand.16-0992>.
- [29] F.L. Wang, X.Y. Zhang, J.C. Zhou, Z.N. Shi, B. Dong, J.Y. Xie, Y.W. Dong, J.F. Yu, Y. M. Chai, Amorphous–crystalline FeNi₂S₄@NiFe-LDH nanograsses with molten salt as an industrially promising electrocatalyst for oxygen evolution, *Inorg. Chem. Front.* 9 (2022) 2068–2080, <https://doi.org/10.1039/D2QI00003B>.
- [30] X. Zou, Y. Liu, G.D. Li, Y. Wu, D.P. Liu, W. Li, H.W. Li, D. Wang, Y. Zhang, X. Zou, Ultrafast formation of amorphous bimetallic hydroxide films on 3D conductive sulfide nanoarrays for large-current-density oxygen evolution electrocatalysis, *Adv. Mater.* 29 (2017) 1700404, <https://doi.org/10.1002/adma.201700404>.
- [31] S.J. Xu, Y.N. Zhou, G.P. Shen, B. Dong, Ni(OH)₂ derived from NiS₂ induced by reflux playing three roles for hydrogen/oxygen evolution reaction, *Chin. J. Struct. Chem.* 41 (2022) 2208052–2208057, <https://doi.org/10.14102/j.cnki.0254-5861.2022-0143>.
- [32] K. Srinivas, Y. Chen, B. Wang, B. Yu, X. Wang, Y. Hu, Y. Lu, W. Li, W. Zhang, D. Yang, Metal–organic framework-derived NiS/Fe₃O₄ heterostructure-decorated carbon nanotubes as highly efficient and durable electrocatalysts for oxygen evolution reaction, *ACS Appl. Mater. Interfaces* 12 (2020) 31552–31563, <https://doi.org/10.1021/acsami.0c09737>.
- [33] B.Q. Li, S.Y. Zhang, C. Tang, X. Cui, Q. Zhang, Anionic regulated NiFe(Oxy)Sulfide electrocatalysts for water oxidation, *Small* 13 (2017) 1700610, <https://doi.org/10.1002/sml.201700610>.
- [34] Y. Pan, K. Sun, S. Liu, X. Cao, K. Wu, W.-C. Cheong, Z. Chen, Y. Wang, Y. Li, Y. Liu, D. Wang, Q. Peng, C. Chen, Y. Li, Core-Shell ZIF-8@ZIF-67-derived CoP Nanoparticle-embedded N-doped carbon nanotube hollow polyhedron for efficient overall water splitting, *J. Am. Chem. Soc.* 140 (2018) 2610–2618, <https://doi.org/10.1021/jacs.7b12420>.
- [35] Q. Fu, X. Wang, J. Han, J. Zhong, T. Zhang, T. Yao, C. Xu, T. Gao, S. Xi, C. Liang, L. Xu, P. Xu, B. Song, Phase-junction electrocatalysts towards enhanced hydrogen evolution reaction in alkaline media, *Angew. Chem. Int. Ed.* 60 (2021) 259–267, <https://doi.org/10.1002/anie.202011318>.
- [36] H.Y. Zhao, R.Y. Fan, Z.Y. Zhao, X. Zhang, B. Dong, Q.X. Lv, X. Liu, B. Liu, Y. M. Chai, Precipitation/dissolution equilibrium to achieve trace iron doping on the surface of β-Ni(OH)₂ for electrocatalytic oxygen evolution, *Fuel* 332 (2023), 125780, <https://doi.org/10.1016/j.fuel.2022.125780>.
- [37] C. Kuai, C. Xi, A. Hu, Y. Zhang, Z. Xu, D. Nordlund, C.J. Sun, C.A. Cadigan, R. M. Richards, L. Li, C.K. Dong, X.W. Du, F. Lin, Revealing the dynamics and roles of iron incorporation in nickel hydroxide water oxidation catalysts, *J. Am. Chem. Soc.* 143 (2021) 18519–18526, <https://doi.org/10.1021/jacs.1c07975>.
- [38] H. Wang, W. Zhang, X. Zhang, S. Hu, Z. Zhang, W. Zhou, H. Liu, Multi-interface collaboration of graphene cross-linked NiS-NiS₂-Ni₃S₄ polymorph foam towards robust hydrogen evolution in alkaline electrolyte, *Nano Res.* 14 (2021) 4857–4864, <https://doi.org/10.1007/s12274-021-3445-5>.
- [39] R.Y. Fan, Y.N. Zhou, M.X. Li, J.Y. Xie, W.L. Yu, J.Q. Chi, L. Wang, J.F. Yu, Y. M. Chai, B. Dong, In situ construction of Fe(Co)OOH through ultra-fast electrochemical activation as real catalytic species for enhanced water oxidation, *Chem. Eng. J.* 426 (2021), 131943, <https://doi.org/10.1016/j.cej.2021.131943>.
- [40] Y. Duan, Z.Y. Yu, S.J. Hu, X.S. Zheng, C.T. Zhang, H.H. Ding, B.C. Hu, Q.Q. Fu, Z. L. Yu, X. Zheng, J.F. Zhu, M.R. Gao, S.H. Yu, Scaled-up synthesis of amorphous NiFeMo oxides and their rapid surface reconstruction for superior oxygen evolution catalysis, *Angew. Chem. Int. Ed.* 58 (2019) 15772–15777, <https://doi.org/10.1002/anie.201909939>.
- [41] S.L. Zhang, B.Y. Guan, X.F. Lu, S. Xi, Y. Du, X.W. (David) Lou, Metal atom-doped Co₃O₄ hierarchical nanoplates for electrocatalytic oxygen evolution, *Adv. Mater.* 32 (2020) 2002235, <https://doi.org/10.1002/adma.202002235>.
- [42] B. Wang, C. Tang, H.F. Wang, X. Chen, R. Cao, Q. Zhang, Core-branch CoNi hydroxysulfides with versatily regulated electronic and surface structures for superior oxygen evolution electrocatalysis, *J. Energy Chem.* 38 (2019) 8–14, <https://doi.org/10.1016/j.jechem.2018.12.006>.
- [43] X. Li, Z. Kou, S. Xi, W. Zang, T. Yang, L. Zhang, J. Wang, Porous NiCo₂S₄/FeOOH nanowire arrays with rich sulfide/hydroxide interfaces enable high OER activity, *Nano Energy* 78 (2020), 105230, <https://doi.org/10.1016/j.nanoen.2020.105230>.
- [44] K.L. Yan, J.F. Qin, Z.Z. Liu, B. Dong, J.Q. Chi, W.K. Gao, J.Q. Lin, Y.M. Chai, C. G. Liu, Organic-inorganic hybrids-directed ternary NiFeMoS anemone-like nanorods with scaly surface supported on nickel foam for efficient overall water splitting, *Chem. Eng. J.* 334 (2018) 922–931, <https://doi.org/10.1016/j.cej.2017.10.074>.
- [45] X. Liu, K. Ni, B. Wen, R. Guo, C. Niu, J. Meng, Q. Li, P. Wu, Y. Zhu, X. Wu, L. Mai, Deep reconstruction of nickel-based precatalysts for water oxidation catalysis, *ACS Energy Lett.* 4 (2019) 2585–2592, <https://doi.org/10.1021/acscenergylett.9b01922>.
- [46] X. Shang, K.L. Yan, Y. Rao, B. Dong, J.Q. Chi, Y.R. Liu, X. Li, Y.M. Chai, C.G. Liu, In-situ cathodic activation of V-incorporated Ni_xS_y nanowires for enhanced hydrogen evolution, *Nanoscale* 9 (2017) 12353–12363, <https://doi.org/10.1039/C7NR02867A>.
- [47] X.Y. Zhang, Y.R. Zhu, Y. Chen, S.Y. Dou, X.Y. Chen, B. Dong, B.Y. Guo, D.P. Liu, C. G. Liu, Y.M. Chai, Hydrogen evolution under large-current-density based on fluorine-doped cobalt-iron phosphides, *Chem. Eng. J.* 399 (2020), 125831, <https://doi.org/10.1016/j.cej.2020.125831>.
- [48] S. Siracusan, V. Baglio, N. Van Dijk, L. Merlo, A.S. Arico, Enhanced performance and durability of low catalyst loading PEM water electrolyser based on a short-side chain perfluorosulfonic ionomer, *Appl. Energy* 192 (2017) 477–489, <https://doi.org/10.1016/j.apenergy.2016.09.011>.
- [49] M.J. Jang, S.H. Yang, M.G. Park, J. Jeong, M.S. Cha, S.H. Shin, K.H. Lee, Z. Bai, Z. Chen, J.Y. Lee, S.M. Choi, Efficient and durable anion exchange membrane water electrolysis for a commercially available electrolyzer stack using alkaline electrolyte, *ACS Energy Lett.* 7 (2022) 2576–2583, <https://doi.org/10.1021/acscenergylett.2c01049>.
- [50] L. Zeng, K. Sun, X. Wang, Y. Liu, Y. Pan, Z. Liu, D. Cao, Y. Song, S. Liu, C. Liu, Three-dimensional-networked Ni₂P/Ni₃S₂ heteronanoflake arrays for highly enhanced electrochemical overall-water-splitting activity, *Nano Energy* 51 (2018) 26–36, <https://doi.org/10.1016/j.nanoen.2018.06.048>.
- [51] M.E. Fleet, The crystal structure of α-Ni₇S₆, *Acta Crystallogr. B* 28 (1972) 1237–1241, <https://doi.org/10.1107/S0567740872004029>.
- [52] F. Lai, J. Feng, T. Heil, Z. Tian, J. Schmidt, G.C. Wang, M. Oschatz, Partially delocalized charge in Fe-doped NiCo₂S₄ nanosheet–mesoporous carbon-composites for high-voltage supercapacitors, *J. Mater. Chem. A* 7 (2019) 19342–19347, <https://doi.org/10.1039/C9TA06250E>.
- [53] Y. Xin, X. Kan, L.Y. Gan, Z. Zhang, Heterogeneous bimetallic phosphide/sulfide nanocomposite for efficient solar-energy-driven overall water splitting, *ACS Nano* 11 (2017) 10303–10312, <https://doi.org/10.1021/acsnano.7b05020>.